The Astrophysical Journal Letters, 1001:L8 (15pp), 2026 April 10 https://doi.org/10.3847/2041-8213/ae4975
© 2026. The Author(s). Published by the American Astronomical Society.
OPEN ACCESS

Sodium-rich Particle as Evidence of Recent and Intense Micrometeoroid Bombardment on Asteroid Ryugu

E. Palomba[1], G. Pratesi[2], M. Angrisani[1], X. Shehaj[2,3], F. Dirri[1], A. Longobardo[1], D. Fulvio[4], S. Caporali[5], and B. Cortigiani[5]
[1] INAF-Istituto di Astrofisica e Planetologia Spaziali, Rome, Italy; ernesto.palomba@inaf.it
[2] Dipartimento di Scienze della Terra, University of Florence, Florence, Italy
[3] Dipartimento di Fisica, University of Trento, Trento, Italy
[4] INAF-Osservatorio Astrofisico di Catania (INAF-OACT), Italy
[5] Dipartimento di Chimica, University of Florence, Florence, Italy
Received 2025 December 1; revised 2026 February 16; accepted 2026 February 18; published 2026 April 2

Abstract

The Hayabusa2 spacecraft returned regolith particles of the near-Earth asteroid Ryugu. We investigated two of these particles and found differences in space weathering by-products, including chemical abundance, redox state, and surface morphology. The more weathered particle shows widespread evidence of microimpacts and, within its outermost surface layers (<10 nm), a pronounced enrichment in sodium (a volatile element), likely vapor deposited during micrometeoroid impacts. The preservation of this ultrathin volatile-rich layer in the harsh space environment suggests that Ryugu's surface experienced an intense micrometeoroid bombardment, possibly within the past ∼1000 yr. These findings underscore the role of meteoroid streams and associated outbursts in driving the space weathering of planetary surfaces.

Unified Astronomy Thesaurus concepts: Small Solar System bodies (1469); Near-Earth objects (1092)

1. Introduction

Space weathering, primarily driven by solar wind irradiation and micrometeoroid bombardment, is a fundamental process that progressively modifies the physical, chemical, and optical properties of the surfaces of airless bodies (B. Hapke 2001; B. E. Clark et al. 2002; C. M. Pieters & S. K. Noble 2016). Notably, micrometeoroids play a crucial role by delivering localized, high-energy impacts that cause micro-scale melting, cratering, vaporization, and redeposition, profoundly altering the microstructure and composition of the regolith (L. P. Keller & D. S. McKay 1993; M. Anand et al. 2004; Y. Wu et al. 2017; M. Matsuoka et al. 2020; D. Fulvio et al. 2021). In contrast, solar wind irradiation mainly induces gradual radiation damage, amorphization, and the possible formation of nanophase metallic iron (npFe^0) particles (M. J. Loeffler et al. 2009; L. P. Keller et al. 2021; D. L. Laczniak et al. 2021; B. W. Denevi et al. 2023; D. L. Laczniak et al. 2024).

On silicate-rich anhydrous bodies such as the Moon and the S-type asteroid Itokawa, this combination of processes has been shown to produce microcraters, amorphous rims, npFe^0, and vapor-deposited coatings (L. P. Keller & D. S. McKay 1993; T. Noguchi et al. 2011; M. S. Thompson et al. 2014; B. W. Denevi et al. 2023). However, for volatile-rich carbonaceous asteroids (C type), the specific role and products of micrometeoroid bombardments and their impact on surface volatile elements remain poorly understood.

The near-Earth asteroid (162173) Ryugu, explored by the Hayabusa2 mission between 2018 June and 2019 November, provides a unique opportunity to investigate these intricate processes (S. Watanabe et al. 2017). The mission returned surface and subsurface samples to Earth on 2020 December 6, collected during two touchdown (TD) operations (T. Yada et al. 2022). The first (TD1) gathered surface material stored in chamber A, while the second (TD2) retrieved particles possibly from depths up to ∼1 m below the surface near an artificial impact crater, stored in chamber C (T. Yada et al. 2022). This stratified sampling enables a direct comparison of regolith exposed to space with material potentially shielded from micrometeoroid impacts and solar wind irradiation. In this study, we investigate two representative Ryugu particles, one from chamber A (A0226), reflecting surface exposure, and one from chamber C (C0242), likely derived from the subsurface. To characterize the effects of space weathering across different scales, we combine Field Emission Gun Scanning Electron Microscopy (FEG-SEM) for micro- to nanoscale surface features and X-ray Photoelectron Spectroscopy (XPS) to probe the chemical state and composition of the outermost atomic layers (<10 nm). Together, these complementary techniques allow us to unravel how space weathering processes uniquely modify the surface of volatile-rich asteroids like Ryugu.

2. Sample and Methods

In this study, we analyzed two millimeter-sized particles collected from the first (A0226) and second (C0242) TD sites by the Hayabusa2 spacecraft on asteroid Ryugu. The particles were allocated to our group during the second "Announcement of Opportunity" by the Japan Aerospace Exploration Agency (JAXA).

2.1. Sample Preparation

Sample preparation and opening were conducted at the DAFNE-Light synchrotron laboratory of the INFN—Frascati National Laboratories (Rome, Italy). A dedicated clean room was established, equipped with a glove box to ensure a controlled environment. The Ryugu particles were transferred from their original sample container (M. Ito et al. 2020) and

Original content from this work may be used under the terms of the Creative Commons Attribution 4.0 licence. Any further distribution of this work must maintain attribution to the author(s) and the title of the work, journal citation and DOI.

mounted on a specifically designed sample holder (SH) and sample holder container (SHC) developed for this study (X. Shehaj et al. 2025). The mounting process was performed inside the glove box under a pure nitrogen atmosphere to minimize terrestrial contamination. The particles were manipulated with a clean steel precision tweezer to avoid contact with the surface region of interest. Due to the friable nature of the Ryugu particles, a submillimeter fragment (<1 mm) was accidentally detached from the main A0226 particle (2 mm) and was therefore excluded from this study.

The millimeter-sized particles C0242 (∼1.7 mm) and A0226 (∼2 mm) were mounted using noninvasive procedures. No additional sample preparation or procedures that could potentially contaminate the surface were applied.

A pure molybdenum wire (50 μm in diameter) and a sintered alumina plate (Al_2O_3) are used following the procedure proposed by X. Shehaj et al. (2025). The mounting configuration is shown in Figure A1 in the Appendix. As noted by L. P. Keller & D. S. McKay (1993), volatile elements (e.g., Na and S) can be mobilized during electron microscope analyses (e.g., FEG-SEM-energy-dispersive X-ray spectrometer, EDS), which could introduce analytical artifacts and affect the chemical results. To mitigate these issues, we began our measurements with XPS, which employs a soft X-ray source, reducing the mobility of volatile elements. Subsequently, the analysis proceeded with FEG-SEM. This approach minimizes the risk of physical or chemical changes, ensuring accurate surface characterization and reliable results.

2.2. X-Ray Photoelectron Spectroscopy

XPS provides elemental and chemical state information from the outermost atomic layers (<10 nm) of the investigated sample surface. In this study, the acquired spectra are considered representative of the entire surface of each Ryugu particle (A0226 and C0242). Surface chemical analyses were performed in the Material Characterization Laboratory (MATCHLAB) of the Università degli Studi di Firenze, Florence, Italy. We used a conventional (nonfocused) X-ray source to preserve the pristine state of the Ryugu particles. The photoelectron spectra were acquired by a PREVAC standard PSE system equipped with a nonmonochromatic X-ray source Mg K-alpha (1253.6 eV) and hemispherical electron energy analyzer EA15. The samples were introduced in the XPS prechamber using a portable glove box under a pure nitrogen (N_2) atmosphere. The samples were kept in ultrahigh vacuum conditions for 2 days to achieve the 10^{-9} mbar vacuum value. The pressure was kept under $2{\cdot}10^{-9}$ mbar during the measurements, and the X-ray source operated at 120 W power (12 kV and 10 mA).

The photoelectrons were collected perpendicular to the sample surface, and the investigated area was about 1.7 × 2 mm with a fixed pass energy of 44 eV. High-resolution Na 1 s (1080–1060 eV); S 2p (166–158 eV); and Si 2p, Fe 3 s, and Mg 2 s (collected in the same region; 109–85 eV) spectra were acquired to quantify the different surface chemical composition for both particles. The Fe 2p (734–702 eV) spectrum was instead acquired for the chemical state quantification.

The spectra were calibrated using the Si 2p transition of silicates at 102.5 eV (C. Elmi et al. 2016). Notably, the adventitious C 1 s signal in the Ryugu samples is very weak and challenging to recognize, making it unsuitable as an internal binding energy (BE) reference, unlike the meteorite samples (e.g., D. L. Laczniak et al. 2021). All data processing and curve fitting were performed using CasaXPS software, version 2.3.5. The inelastic background was subtracted using Shirley's method (D. A. Shirley 1972).

The peak related to the $Fe2p_{3/2}$ transition was used to quantify the chemical state by the M. C. Biesinger et al. (2011) fitting procedures. The deconvolution of XPS spectra was performed by combining Gaussian and Lorentzian functions (70/30 ratio). The relative chemical quantification was calculated considering each element's peak area and atomic sensitivity factors (J. Chastain & R. C. King 1992).

2.3. Scanning Electron Microscopy

Measurements were conducted using a Thermo Scientific Apreo FEG-SEM at the Centre for Electron Microscopy—Eindhoven Nanoport, Netherlands. The samples were transferred from our SHC to the Thermo Scientific™ CleanConnect™ Sample Transfer System using a glove box (in pure Ar atmosphere) in the same center. The high-resolution images were acquired by secondary electron (SE) mode in variable vacuum conditions (10^{-3}–10^{-5} mbar) with an accelerating voltage of 1 kV and a beam current of 6.3 pA. Elemental maps were acquired by EDS operating at 10 kV accelerating potential and 1.6 nA probe currents, with 8000 cps as the average count rate on the whole spectrum and a counting time of 300 s.

3. Results

3.1. Surface Morphologies

Electron microscopy revealed distinct morphological differences between the surfaces of the two Ryugu particles, A0226 and C0242 (Figures 1–3 and Figures A1–A5 in the Appendix). In particular, A0226 exhibits abundant micro- to nanometer-scale impact craters, localized melt deposits, and an extensively vesiculated surface (Figures 1–2 and Figures A2–A4 in the Appendix). In contrast, C0242 remains largely pristine, characterized by a smooth surface topography and mineralogy not affected by impact-related processes (Figure 3 and Figures A3–A5 in the Appendix).

Among the impact-related features observed in A0226, two remarkable examples highlight the pervasive effects of space weathering. The first is a prominent crater-like structure, exceeding 40 μm in size (Figure 1), composed mainly of iron sulfides and quenched silicate glass, forming a complex melt emulsion with a highly vesicular texture (Figure 1). The second example is an unusual drop-splash impact structure: an irregular melt-derived droplet approximately 2 μm in diameter, distinguished by a central cavity with a fluidal, flow-like morphology (Figure 2). It rests discordantly atop a frothy, vesiculated surface, suggesting an impact-related depositional process. This subspherical, droplet-splash impact object consists of quenched silicate glass, with iron sulfides enriched around the central cavity, and is further surrounded by submicron secondary impact craters (Figures 2(c)–(e)). Additional melt splash deposits of varying size and geometry are commonly observed on the A0226 surface (Figure A2 in the Appendix).

Further evidence for the contrasting surface evolution of the two Ryugu particles is provided by the pronounced differences in morphologies of framboidal magnetite observed in A0226 and C0242 (Figure 3). In A0226, framboids that

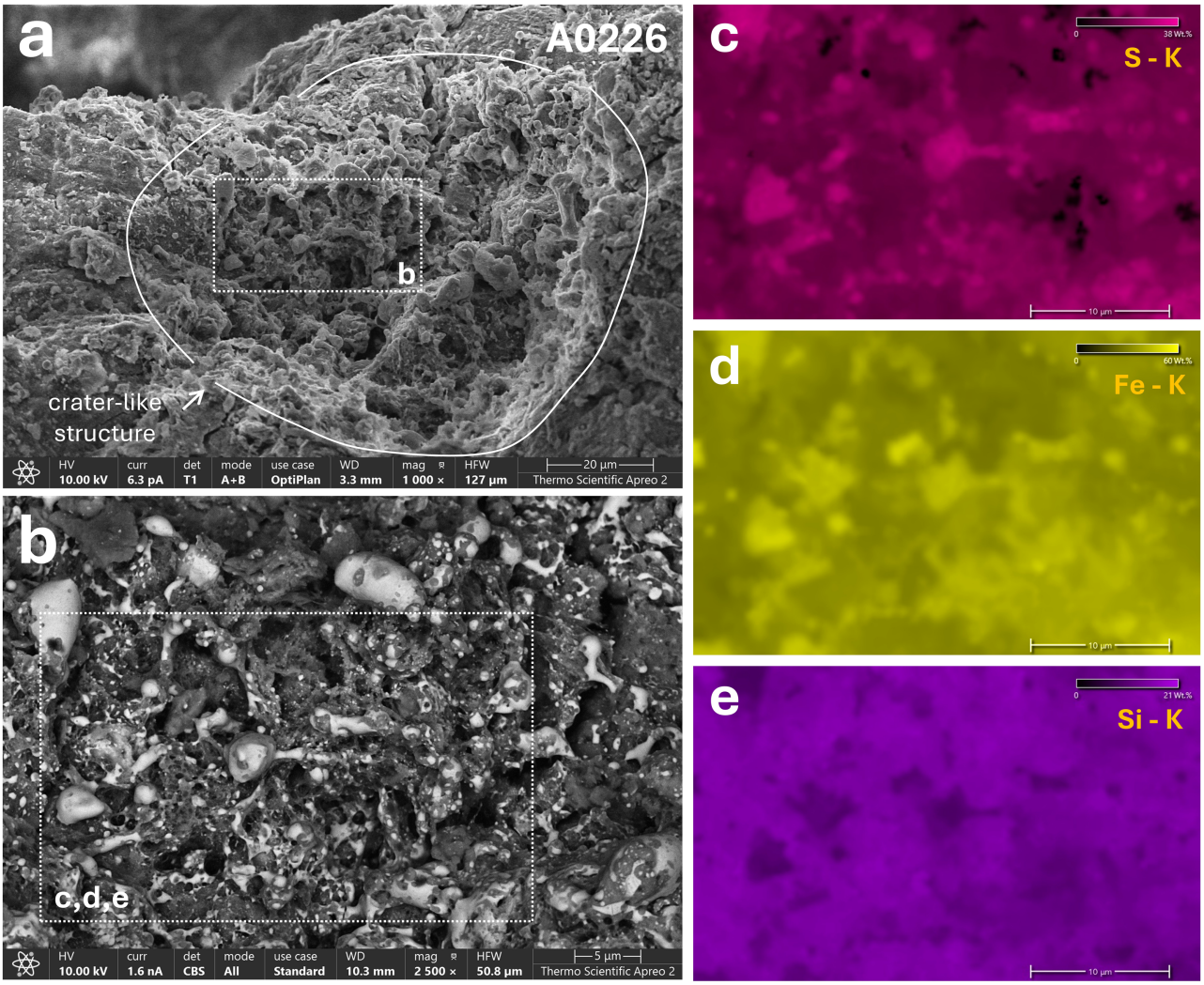

Figure 1. Electron microscope images and chemical maps of the crater-like structure observed on the A0226 surface. (a) Panoramic SE image of the impact-crater-like structure, outlined by the continuous curvilinear white line. The white dashed rectangle indicates the area shown at high magnification in panel (b), which presents the internal crater-like structure in electron backscattered mode. (c)–(e) FEG-SEM-EDS element maps of the same region (highlighted in Figure 1(b)) for sulfur (S, k-line), iron (Fe, k-line), and silicon (Si, k-line), respectively.

would originally display the dodecahedral habitus typical of pristine magnetite aggregates have instead become more spheroidal, with a granular surface texture that is commonly pitted by submicron-scale impact craters (Figures 3(a) and (c)). In addition, an interconnected network of ultrathin films, possibly silicate and on the order of tens of nanometers thick, spans adjacent magnetite grains, producing a characteristic "cobweb" texture that locally incorporates quenched splash ejecta (Figure 3(c)). By contrast, framboidal magnetite in C0242 largely retains its pristine geometry and smooth surfaces and is commonly associated with phyllosilicate sheets (Figures 3(b) and (d)).

These morphological differences also extend to the phyllosilicate-rich matrix, the dominant lithology in Ryugu samples, which accounts for ∼80 vol.% (A. Yamaguchi et al. 2023). In C0242, the matrix occurs as pristine lamellar sheet aggregates (Figures A3 and A5 in the Appendix), whereas in A0226, it displays a frothy surface texture consistent with partial melting and vesiculation processes (Figures A2 and A3 in the Appendix). Likewise, pyrrhotite grains in A0226 commonly exhibit roughened, vesicular surfaces, in contrast to the smooth, largely intact pyrrhotite grains typical of C0242 (Figures A3 and A4 in the Appendix).

3.2. Surface Chemical Composition

We performed XPS analyses to investigate compositional differences in the outermost layers (<10 nm; see Section 2.2) of the entire surfaces of each Ryugu particle, A0226 and C0242. The resulting photoelectron spectra reveal marked differences in relative elemental abundances between the two samples (Figures 4–5; Figures A6–A8 and Table A1 in the Appendix). Notably, A0226 exhibits substantial enrichment in volatile elements, particularly sodium and sulfur, compared to C0242 (Figures 4 and A6 in the Appendix). High-resolution Na 1 s spectra indicate that the A0226 surface contains nearly 5 times more sodium than C0242 (atomic percentage ratio A0226/C0242 = 4.8 ± 1.0; Figures 4 and 5). Sulfur is detected in A0226, while in C0242, it is below the detection limit. These observations indicate a preferential enrichment of volatile species on the surface of A0226 (Figures 5 and A6 in the Appendix). Comparison of other major elements

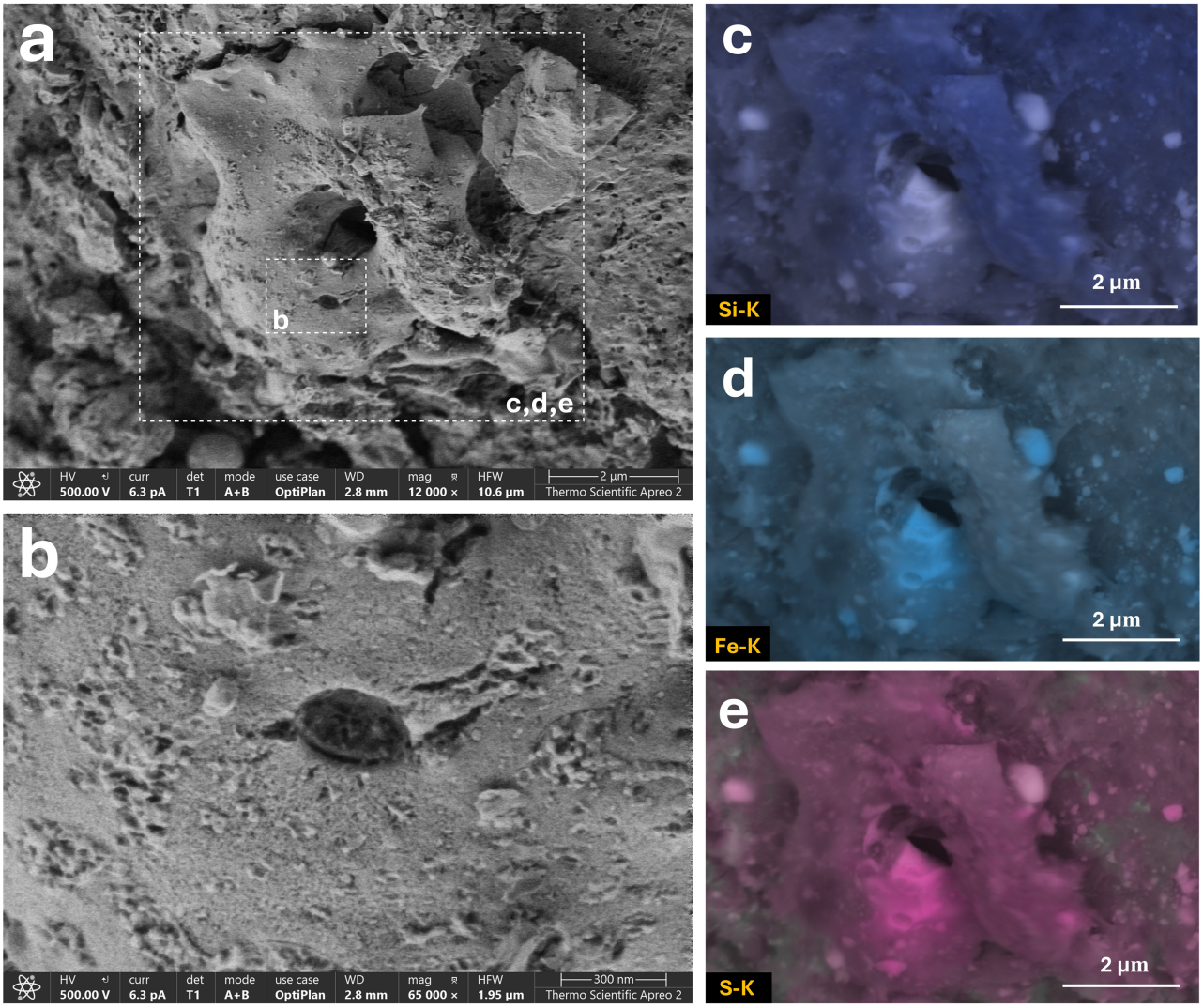

Figure 2. Electron microscope images and chemical maps of drop-melt splash impact structure observed on the A0226 surface. (a) Panoramic image in SE mode. (b) Higher-magnification view of the heavily cratered surface. (c)–(e) FEG-SEM-EDS element maps of the same region, overlapped with the drop-melt splash impact structure: (c) silicon (Si, k-line), (d) iron (Fe, k-line) and (e) sulfur (S, k-line).

(Mg 2s, Fe 3s, and Si 2p) further highlight pronounced contrasts between the two particles (Figures 5 and A7 in the Appendix). Relative to C0242, A0226 is depleted in Mg (0.5 ± 0.1) and enriched in Fe (1.9 ± 0.1) and Si (1.1 ± 0.1). High-resolution Fe 2p transition spectra also reveal variations in Fe redox states (Figure A8 in Appendix). The Fe $2p_{3/2}$ peak maximum for A0226 occurs at 710.2 eV, slightly lower than that of C0242 (710.6 eV), reflecting a different local chemical environment. Quantitative fitting, following the approach of M. C. Biesinger et al. (2011), provide evidence that both Fe(II) and Fe(III) states contribute to the multiple structure, possibly associated with iron oxides and silicate phases. The $Fe^{3+}/\Sigma Fe_{tot}$ ratio decreases by nearly 10% from C0242 to A0226, suggesting that Fe (III) has been reduced to Fe (II) in A0226's surface layers.

4. Discussion

4.1. Space Weathering Signatures

Electron microscope analyses reveal that particle A0226 exhibits widespread microimpact structures, including micro-craters and associated melt splashes with nearby ejecta. In contrast, these features are not observed on the surface of C0242, as shown in the comparison in Figures A1–A5 in the Appendix. Pyrrhotite crystals in C0242 generally appear pristine (Figures A3 and A4 in the Appendix), whereas those in A0226 display roughened, vesiculated surfaces attributed to space weathering processing (A. Nakato et al. 2023; D. Harries et al. 2024). The remarkable crater-like structure larger than 40 μm in size, observed on the A0226 surface, suggests that an energetic microimpact event may have melted the precursor material (Figure 1). The presence of a complex emulsion of quenched silicate glass, Fe sulfide, and vesicles on the affected surface indicate temperature likely exceeding 1700 K (C. Hamann et al. 2018), followed by rapid cooling, consistent with energetic microimpacts similar to those described in T. Matsumoto et al. (2018). Additionally, the drop-like melt splash impact on the A0226 surface (Figure 2) may instead indicate a low-speed micrometeorite impact that generated a fluid-plastic deformation regime that rapidly solidified during the ejecta's evolution. This unique structure could have formed through the combined effect of a low-energy impact and the asteroid's low gravity, allowing the melt to solidify before the ejecta settled onto the surrounding surface.

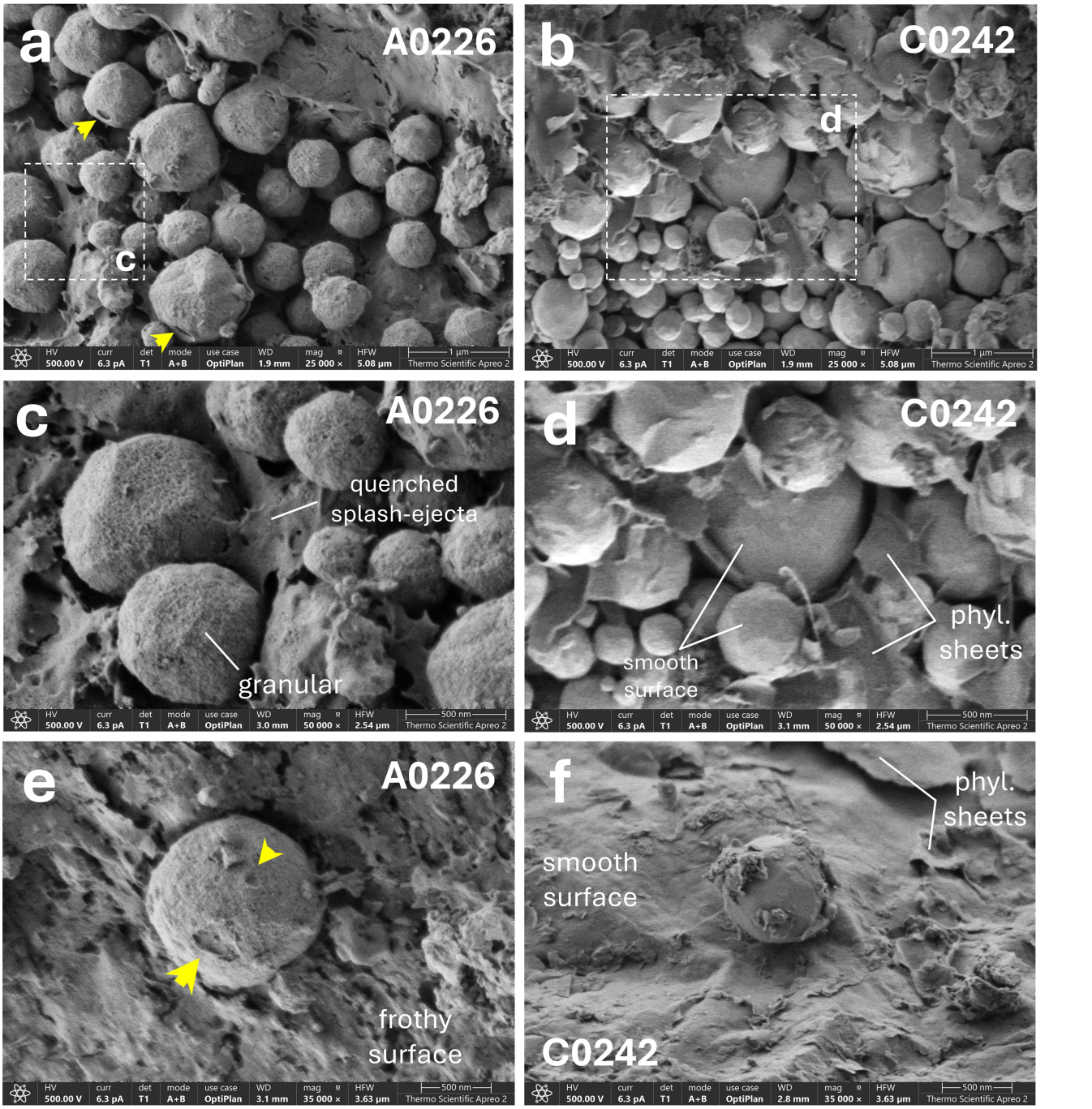

Figure 3. Electron microscope images in secondary electron (SE) mode of magnetite grains in A0226 and C0242 particle surfaces. (a) Panoramic SE image of framboidal magnetite on the A0226 surface, showing micro- to nano-impact craters (highlighted by yellow arrows), granular surface morphology, and magnetite grains interconnected by a "cobweb" texture. (b) Panoramic SE image of framboidal magnetite on the C0242 surface, showing a pristine, smooth morphology commonly associated with phyllosilicate (phyl.) sheets. (c) High-magnification view of the area in panel (a), highlighting quenched splash ejecta feature on weathered magnetite. (d) High-magnification view of the area in panel (b), showing a smooth magnetite surface and associated phyllosilicate sheets. (e) Individual magnetite grain in A0226 exhibiting nanometer impact craters on a frothy surface. (f) Individual magnetite grain in C0242 showing a smooth surface on a phyllosilicate-rich matrix.

The presence of low-velocity impacts is not unexpected, given previous evidence that suggest they are pervasive on Ryugu (N. Tomioka et al. 2023). This structure emerges from an extensive frothy surface, which likely formed earlier through the combined effects of solar wind irradiation and micrometeoroid impacts. Solar wind gas species (e.g., He, H) were possibly implanted into the regolith and subsequently released through localized heating, probably triggered by micrometeoroid impacts. These processes liberated the implanted gases, forming the blisters typically observed on a frothy surface (T. Noguchi et al. 2023). Frothy textures are common and widely distributed across the A0226 surface (e.g., Figures A2 and A3 in the Appendix) and strongly resemble the high-blister textures produced by micrometeoroid impact simulations (A. J. López-Oquendo et al. 2024). The occurrence of quenched splash ejecta with "cobweb" textures among

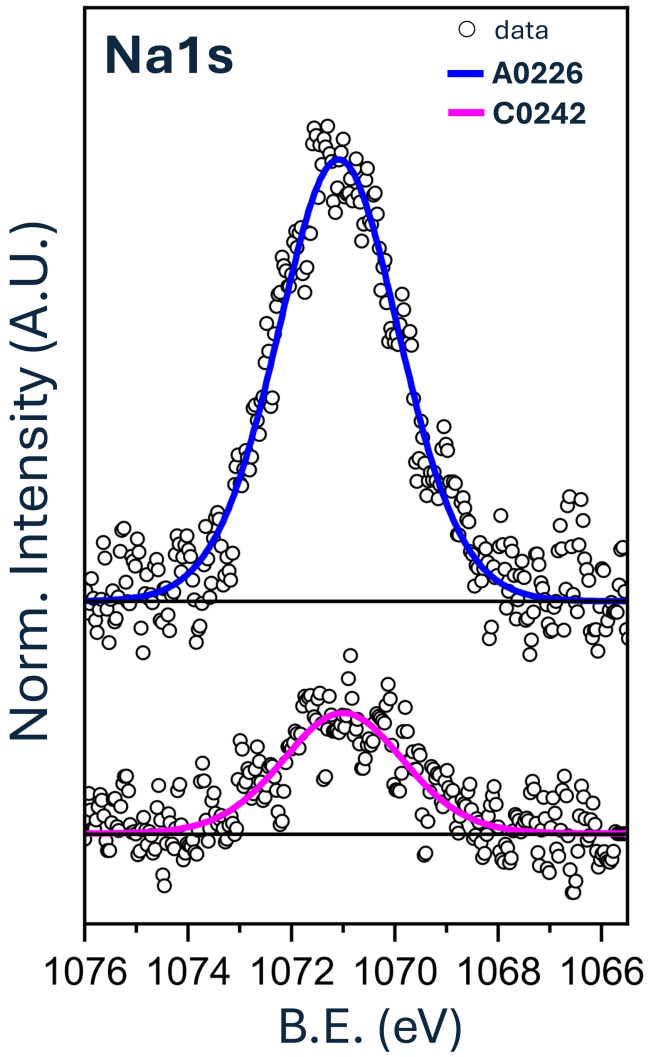

Figure 4. Comparison of sodium (Na 1 s) photoelectron spectra. Normalized high-resolution Na 1 s photoelectron spectra of the C0242 and A0226 particles. The A0226 surface exhibits a significant sodium enrichment compared to C0242.

magnetite grains (Figure 3(c)) further supports the idea that impact processes may have melted the precursor material, which was then ejected and rapidly quenched. In contrast, the surface of particle C0242 shows no significant evidence of such processing, as the phyllosilicate-rich matrix and phyllosilicate sheets appears unaltered with a smooth surface, suggesting that C0242 experienced minimal exposure to space weathering. Overall, the morphological differences between A0226 and C0242 likely reflect different residence depths during Ryugu's recent near-Earth phase. Cosmic-ray exposure ages of Ryugu samples are ~5 Ma (R. Okazaki et al. 2023), and resurfacing of the upper ~1 m is expected to be slower in the near-Earth region (~2–8 Ma) than in the main belt (<1 Ma) (M. Matsumoto et al. 2024 and references therein), allowing particles to remain exposed long enough for microimpact and irradiation features to accumulate. A0226 is therefore interpreted to have remained at the Ryugu surface for a significant fraction of this interval, recording the processing described above. In contrast, the absence of comparable features on C0242 is most consistent with shielding by episodic burial or regolith gardening, which would limit

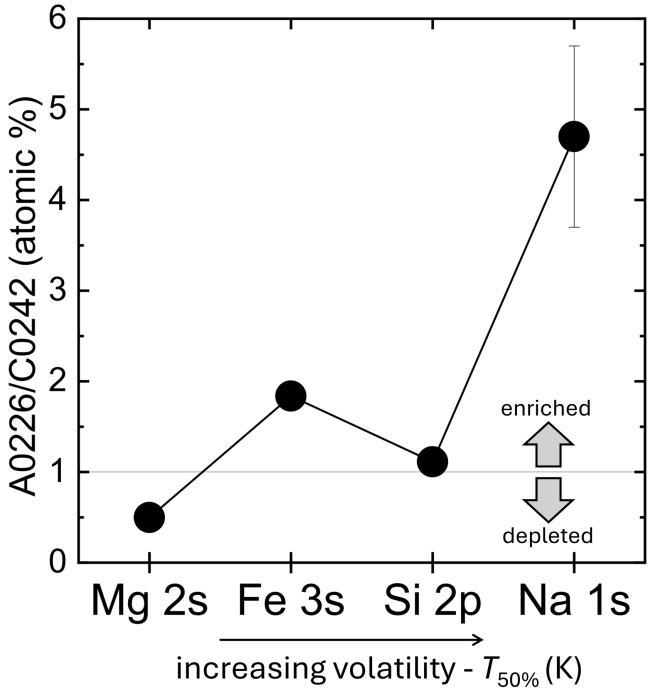

Figure 5. Surface elemental composition of Ryugu particles A0226 and C0242 obtained from XPS measurements. Elemental abundances obtained from high-resolution photoelectron spectra, expressed as A0226/C0242 ratio (in atomic percent). Elements are ordered from left to right by decreasing 50% condensation temperature (B. J. Wood et al. 2019). An A0226/C0242 atomic percentage ratio greater than 1 indicates enrichment on the A0226 surface. Sulfur data were excluded in this diagram since they were below the detection limit in the C0242 particle. All data sources are given in the Appendix data section, and error bars are smaller than symbols.

effective space weathering exposure and preserve its near-pristine surface state. Overall, these observations depict a scenario in which A0226 has been exposed to prolonged space weathering processes, whereas C0242 has remained largely protected in the Ryugu subsurface.

4.2. Near-surface Volatile Enrichment

XPS analyses reveal clear differences in surface chemistry between A0226 and C0242 (Figures 4, 5, A6, A8). Nanoparticles of metallic iron (npFe^0), which can be promoted through the reduction of Fe (II) by solar wind irradiation and microimpacts, are exceptionally rare on Ryugu (T. Noguchi et al. 2023; M. Matsumoto et al. 2024). It has been suggested that hydroxyl groups (–OH) in phyllosilicates may inhibit this reduction (T. Noguchi et al. 2023). The XPS spectra comparison of the surface (<10 nm) composition between the two particles reveals a ~10% decrease in the $Fe^{3+}/\Sigma Fe_{tot}$ ratio from C0242 to A0226, indicating that space weathering processes may promote reduction of Fe(III) to Fe(II) on the surface of A0226. This result is consistent with differences observed between less-weathered and more-weathered particles (T. Noguchi et al. 2023; S. Laforet et al. 2024; M. Matsumoto et al. 2024).

Regarding volatiles, particle A0226 exhibits a marked enrichment of sodium and sulfur within its outermost atomic layers (<10 nm). Energy-dispersive X-ray spectroscopy mapping also identifies localized regions, tens of micrometers in size and associated with impact features, which are enriched in Fe and S (Figures 1(b)–(e)), likely reflecting the presence of

micro- and nanophase iron sulfides (npFeS), consistent with the observations of npFeS-rich films produced by using laser irradiation to simulate microimpact (S. K. Noble et al. 2011).

On airless-body regolith, long-term space weathering driven by solar wind sputtering and related processes is generally expected to cause volatile depletion in the near surface. This includes the loss of Na and S from Na-bearing phases and S-bearing phases (mainly Fe-sulfides), as demonstrated by laboratory irradiation/sputtering experiments and supported by observations of other airless bodies (L. R. Nittler et al. 2001; R. M. Killen 2003; C. A. Dukes et al. 2011; T. Matsumoto et al. 2020, 2021; J. M. Christoph et al. 2022)

For instance, solar wind ions can directly modify npFeS rims and Fe-sulfide grains, preferentially sputtering sulfur; in the case of npFeS rims, this process is accompanied by the development of Fe whiskers and progressive S loss (T. Matsumoto et al. 2020; T. Matsumoto et al. 2021; J. M. Christoph et al. 2022). Consequently, under long-term space weathering conditions, mature regolith surfaces are expected to show Na and S depletion at XPS sampling depths, rather than enrichment. Consistent with this behavior, sulfur depletion attributable to solar wind processing has also been inferred for asteroid surfaces such as Eros and Psyche (L. R. Nittler et al. 2001; R. M. Killen 2003). Similarly, irradiation/sputtering experiments and XPS measurements show that Na is rapidly removed from Na-bearing minerals within the first tens of nanometers (C. A. Dukes et al. 2011).

Observations of Mercury, the Moon, and Phaethon further support this depletion framework, revealing tenuous exospheres sustained by surface-derived Na and S released via sputtering, micrometeorite impacts, and thermal desorption (M. T. Hui 2023; Q. Zhang et al. 2023). The Na and S enrichment observed on A0226 therefore likely reflects a transient, diffuse and non-long-term surface overprint, implying a recent and short-lived resurfacing (or coating) episode on Ryugu's surface.

Micrometeoroid impacts can provide a straightforward mechanism for such a transient overprint: highly localized heating can vaporize Na (and other volatiles) from both target and projectile material, and the resulting vapors ejecta may rapidly redeposit as ultrathin condensate layers on nearby grains, forming volatile-rich skins over more refractory substrates (e.g., L. P. Keller & D. S. McKay 1993). This interpretation is consistent with sodium, sulfur, and micro- and nanophase iron sulfide (npFeS) enrichment observed on A0226. The Mg depletion observed in the A0226 XPS depth profiles (Figure 5) may further reflect burial of Mg-bearing phases beneath a thin Na-/S-rich veneer. Because these coatings are weakly bound and readily removed by solar wind sputtering (and, to a lesser extent, photodesorption; C. A. Dukes et al. 2011), their preservation implies that the volatile enrichment is recent.

4.3. A Meteoroid Stream Outburst Scenario

Experimental and modeling studies indicate that solar wind exposure can remove a large fraction of sodium from Na-bearing minerals, with ~50% lost within 1000 yr, after which a residual fraction (40%–60%) remains relatively stable (e.g., Figures 2 and 5 in C. A. Dukes et al. 2011). Sulfur depletion from Fe sulfides also occurs with similar timescales (up to ~50% within a few years and up to ~90% within $\sim 10^3$ yr; i.e., Figure 9 in J. M. Christoph et al. 2022). The Na- and S-enrichment observed on A0226 is most plausibly interpreted as the residue of a recent event that emplaced an ultrathin volatile-rich veneer on Ryugu's surface. We therefore propose a scenario in which an encounter with a meteoroid stream outburst triggered enhanced bombardment on Ryugu, leading to the extensive production and deposition of impact-generated vapor coatings. Based on the timescales derived from experiments on Na- and S-bearing minerals, this event likely occurred in the very recent past—specifically, on a millennial timescale.

5. Conclusions

Our results indicate that Ryugu's regolith particles have recorded space weathering on multiple, distinct timescales. The pervasive microimpact textures and irradiation-related features on A0226 (absent on C0242) are consistent with near-surface exposure during Ryugu's residence in the near-Earth region within the last ~5 Ma, as suggested by cosmic-ray exposure ages and resurfacing timescales (R. Okazaki et al. 2023; M. Matsumoto et al. 2024). Superimposed on this long-term record, XPS reveals an ultrathin (<10 nm) Na- and S-enriched surface veneer on A0226, which likely reflects a much more recent coating event, with a conservative upper limit of $\sim 10^3$ yr. We interpret this veneer as impact-generated condensate produced by micrometeoroid activity and locally redeposited onto nearby surfaces, temporarily counteracting the steady-state volatile depletion expected under prolonged solar wind exposure. This scenario is plausible given that the Earth is currently impacted by nearly 1200 meteoroid streams (2025 August on IAU Meteor Data Center[6]), and near-Earth objects may intersect analogous trails during their orbital evolution. Some of these streams may generate outbursts with a significant number of impacts, akin to those observed on Earth (P. Jenniskens 2017). An outburst is a short (minutes to hours) but very intense event typically caused by young dust trails that have not yet dispersed into a broad stream (P. Jenniskens 2006). Such events would likely have occurred recently in Ryugu's history, contributing to the resurfacing of its outermost layers. This discovery underscores the importance of outbursts in meteoroid streams as a key factor in space weathering processes, particularly for near-Earth planetary bodies. A more comprehensive understanding of planetary surface evolution should incorporate the role of meteoroid impacts, especially those associated with encounters with meteoroid streams and related outbursts during a planetary object's solar orbit.

Acknowledgments

We thank the AO3 issued by ISAS/JAXA for allocating the Ryugu A0226 and C0242 particles to this research project. These samples are diplayed on the Ryugu Sample Database at https://darts.isas.jaxa.jp/app/curation/ryugu/. The authors gratefully acknowledge review from anonymous reviewers, which improved the quality of this work. The authors thank Dr. Adrian Sandu, Dr. Alice Scarpellini, and Dr. Tiziano Catelani for FEG-SEM support. We thank Prof. Andrea Caneschi and Prof. Matteo Mannini for providing access to the MATCHLAB laboratory facilities at the Università degli Studi

[6] https://bitl.to/5oCS

di Firenze, Florence, Italy. The authors thank Dr. Nicola Calisi for assistance with XPS data processing.

Competing Interests

Authors declare that they have no competing interests.

Data and Materials Availability

All data needed to evaluate the conclusions in the paper are present in the paper and/or the supplementary materials.

Funding

This work was supported by the National Institute of Astrophysics (Italy) as Pristine Returned Sample Testing InvestiGation and Examination (PRESTIGE) project.

Appendix

The appendix includes figures and tables supporting the analysis presented in the main text of the article. It includes eight figures (Figures A1–A8) and one table (Table A1).

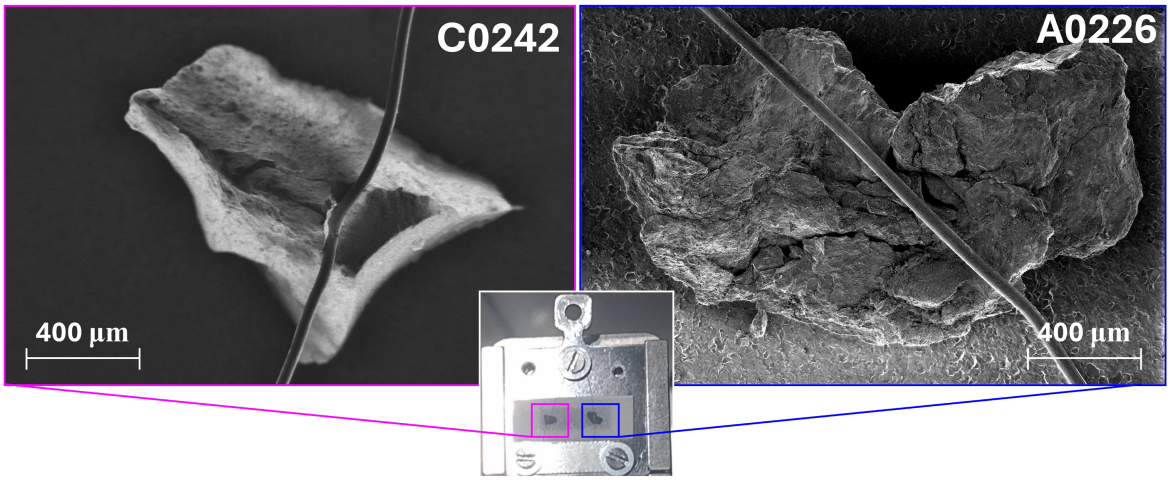

Figure A1. SE images of C0242 (left) and A0226 (right) Ryugu particles and SH configuration (central photo). The particles were mounted between pure molybdenum wire and an alumina (Al_2O_3) plate. The C0242 surface is smooth and unfractured. On the contrary, the A0226 surface is irregular and highly fractured.

Table A1
Elemental Abundances of A0226 and C0242 Ryugu Particles Expressed as Atomic Percentages, Determined from High-resolution XPS Spectra

	A0226	2σ	C0242	2σ
Mg 2s	16	2	32	2
Fe 3s	9.1	0.8	4.9	0.8
Si 2p	70	5	61	4
Na 1s	4.8	0.4	1.0	0.4
S 2p	b.q.l.	...	b.d.l.	...

Note. The data were calculated using literature sensitivity factors (Chastain & King 2011). Errors correspond to the standard deviation (σ) obtained from spectral fitting across all XPS analysis points.
The abbreviation "b.q.l" denotes "below quantification limit," and "b.d.l" denotes "below detection limit."

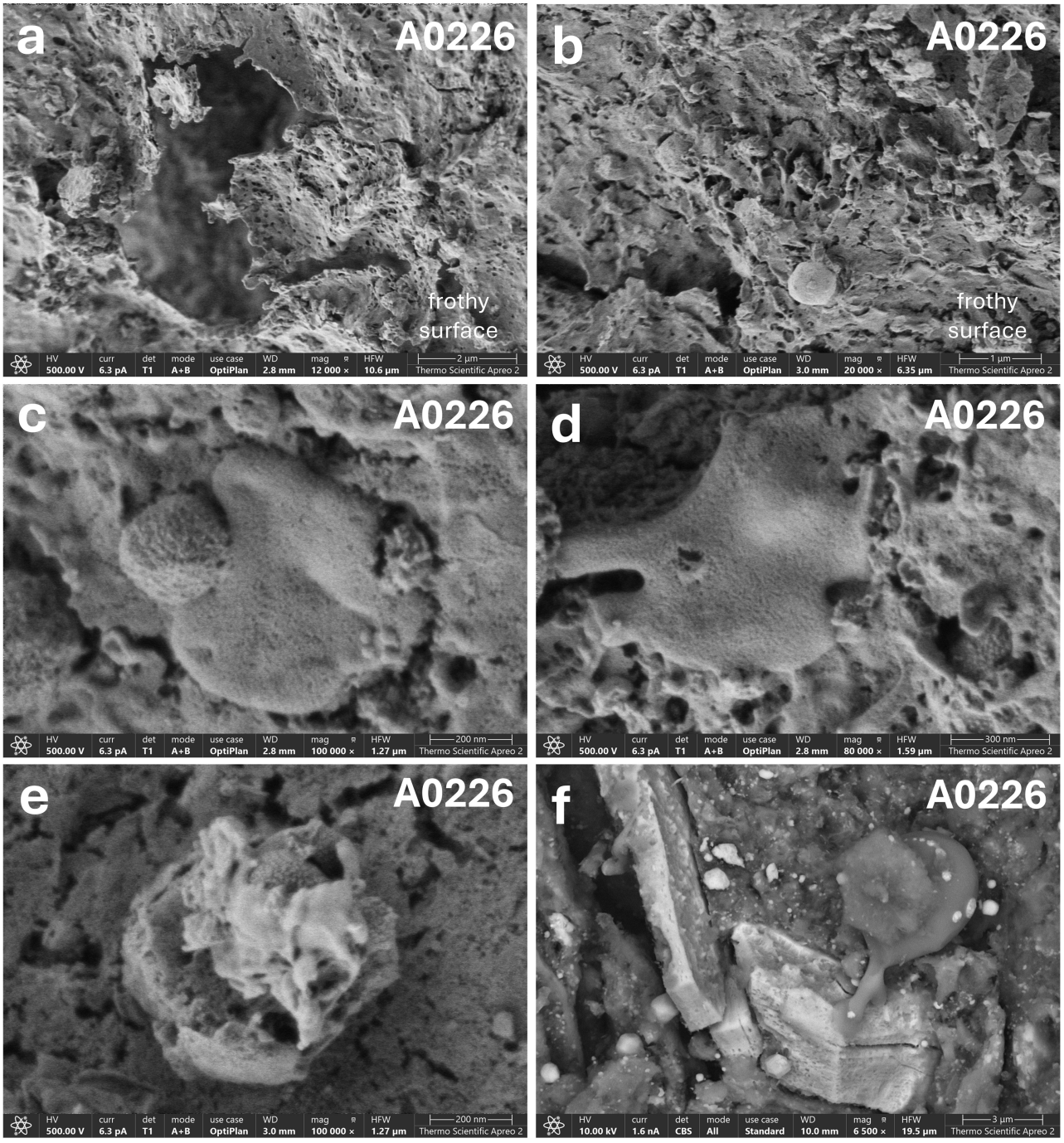

Figure A2. Electron microscope images of frothy surfaces and impact-melt structures on the surface of A0226. (a), (b) Representative frothy surface textures in secondary electron (SE) mode. (c)–(e) Impact-melt deposits with varying sizes and morphologies in SE mode. (f) Melt splash deposits associated with a weathered pyrrhotite grain in backscattered electron (BSE) mode.

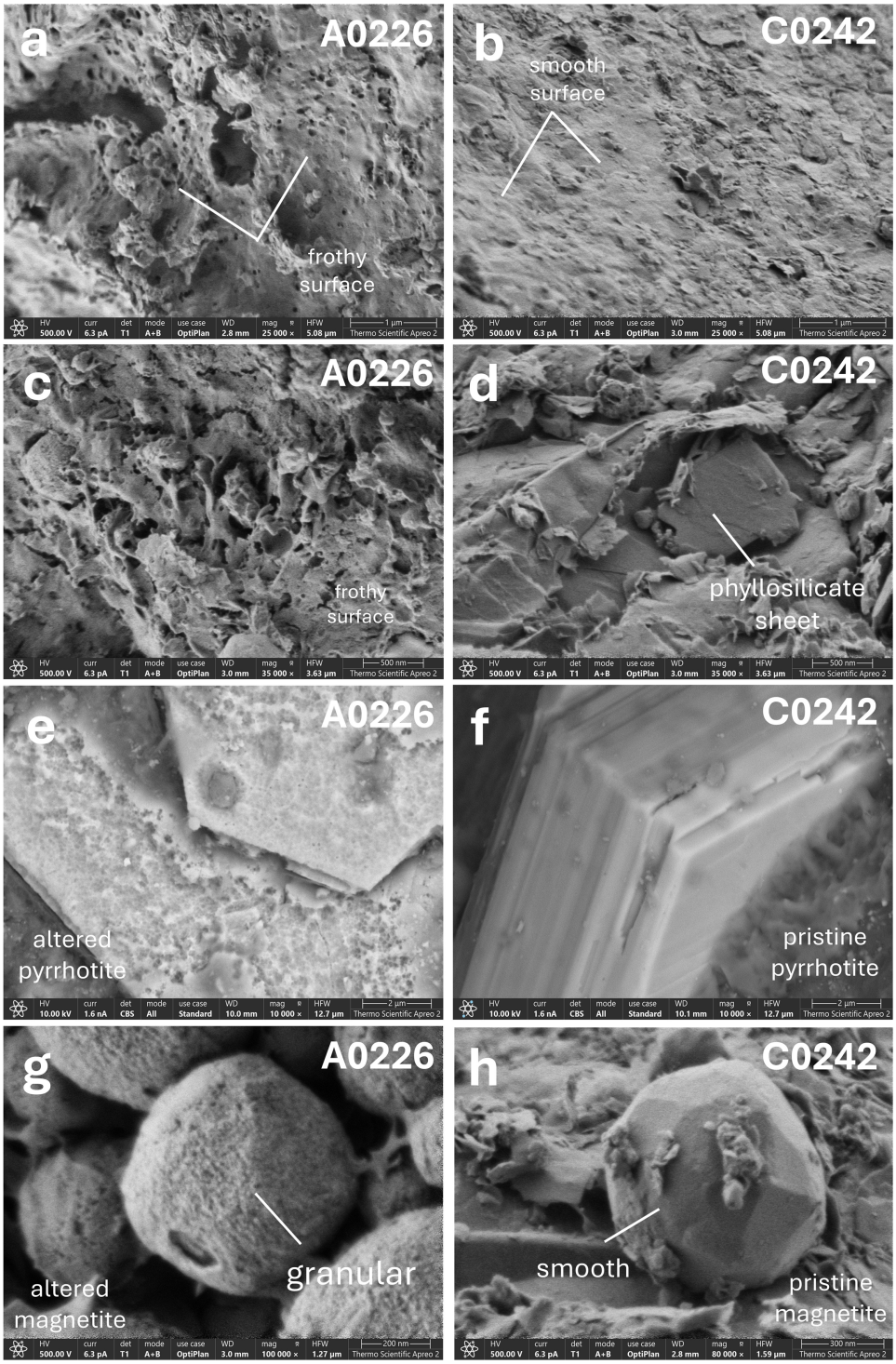

Figure A3. Electron microscope images of C0242 and A0226 particles. (a), (c) Frothy surface of A0266 particle in secondary electron (SE) mode. (b), (d) Smooth phyllosilicate-rich matrix on the surface of C0242 particle in SE mode. (e) Incipient space weathering features on the surface of pyrrhotite grains found in the A0226 surface in BSE mode. (f) Smooth pyrrhotite surface in C0242 particle imaged in BSE mode. (g) Incipient space weathering features on the surface of magnetite grain in A0226 imaged in SE mode. (h) Smooth magnetite grain in C0242 particle imaged in SE mode.

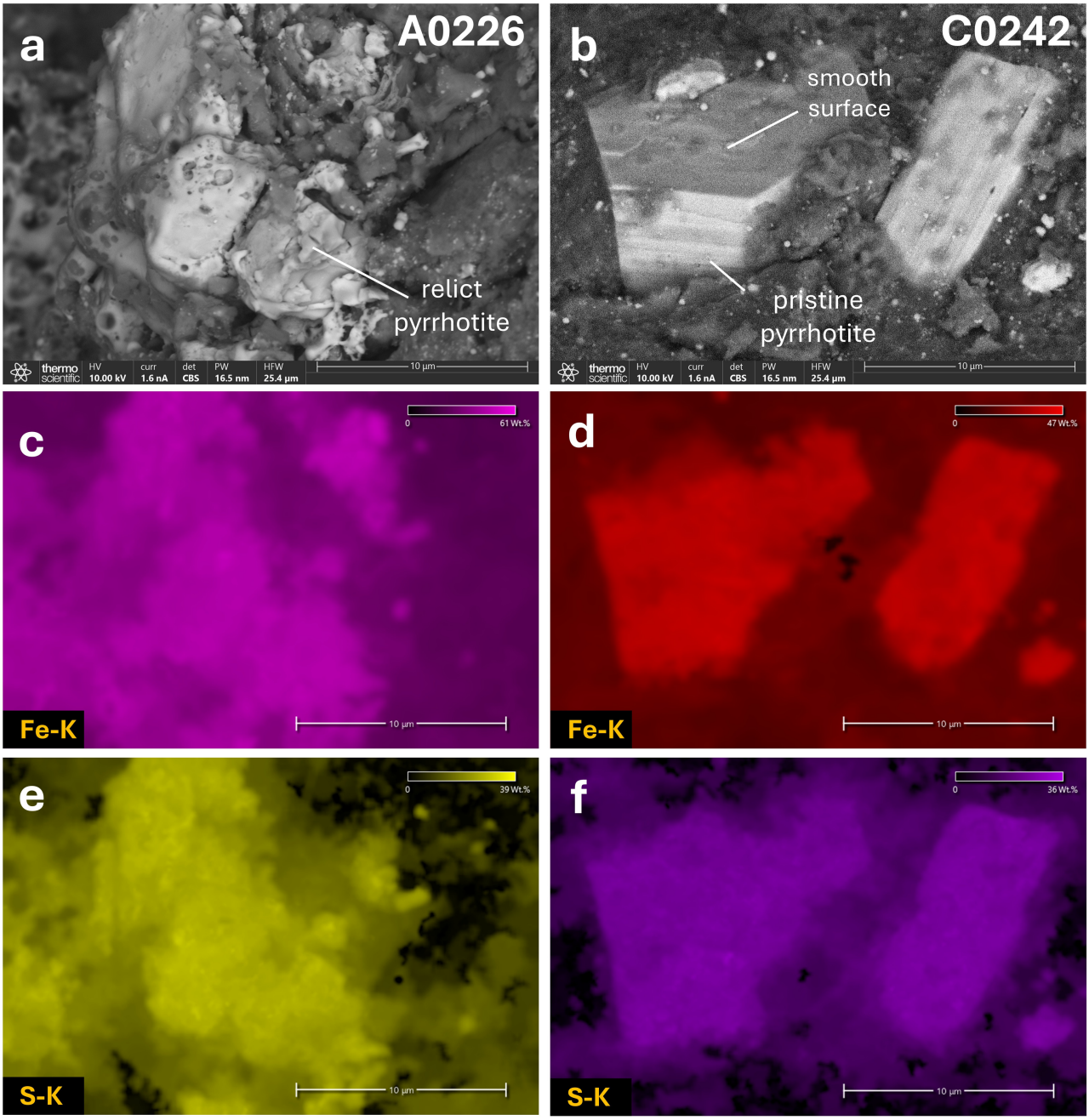

Figure A4. Electron microscope images and FEG-SEM–EDS analyses of pyrrhotite grains on particles A0226 and C0242. (a) Backscattered electron (BSE) image of a relict pyrrhotite grain on the surface of particle A0226, with corresponding Fe-K ((c)) and S-K ((e)) EDS elemental maps. (b) BSE image of a pristine pyrrhotite grain on the surface of particle C0242, with corresponding Fe-K ((d)) and S-K ((f)) EDS elemental maps.

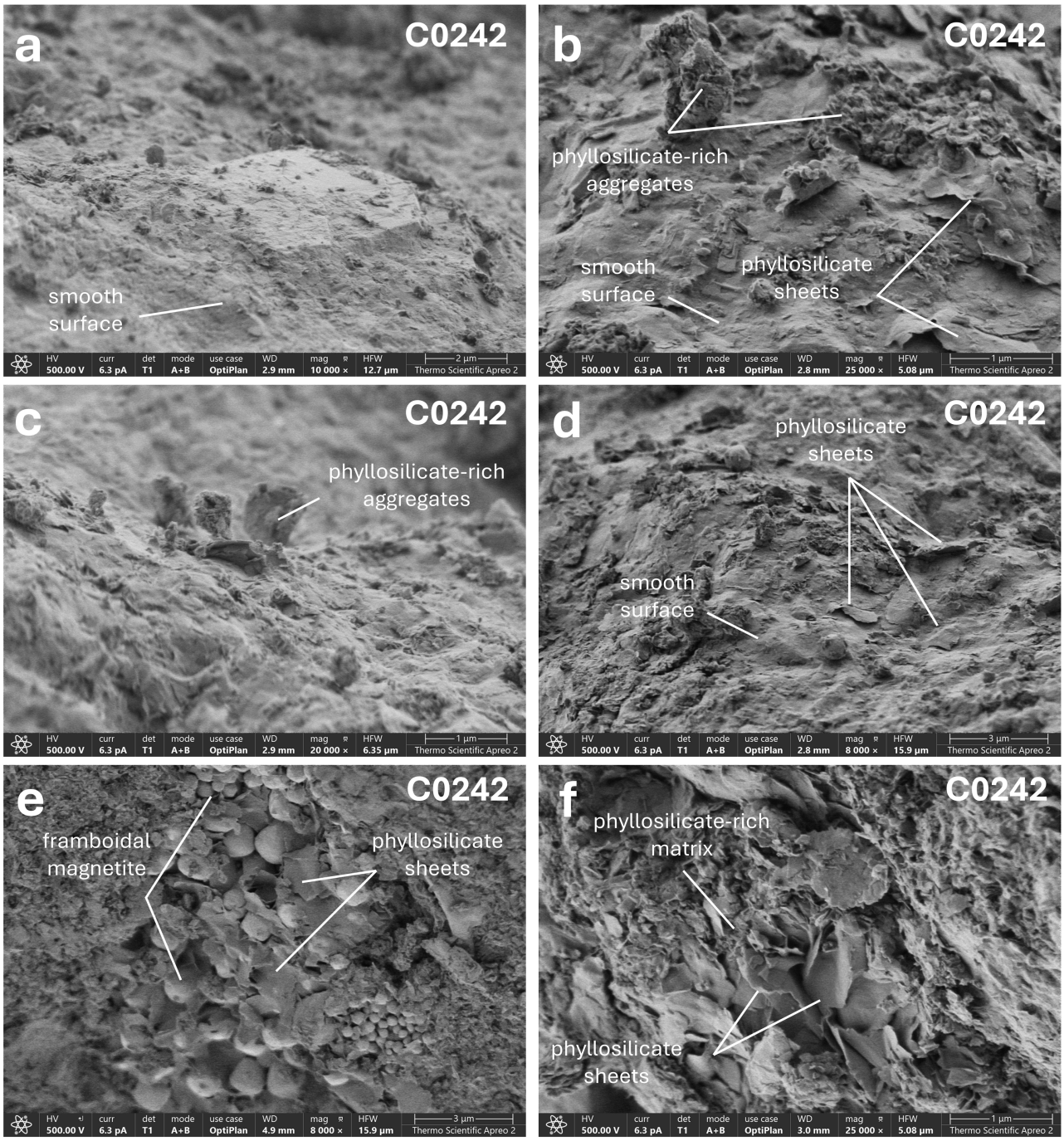

Figure A5. Electron microscope images showing characteristic smooth surfaces and phyllosilicate-rich matrix textures on particle C0242. (a)–(f) Representative SE images of the C0242 surface.

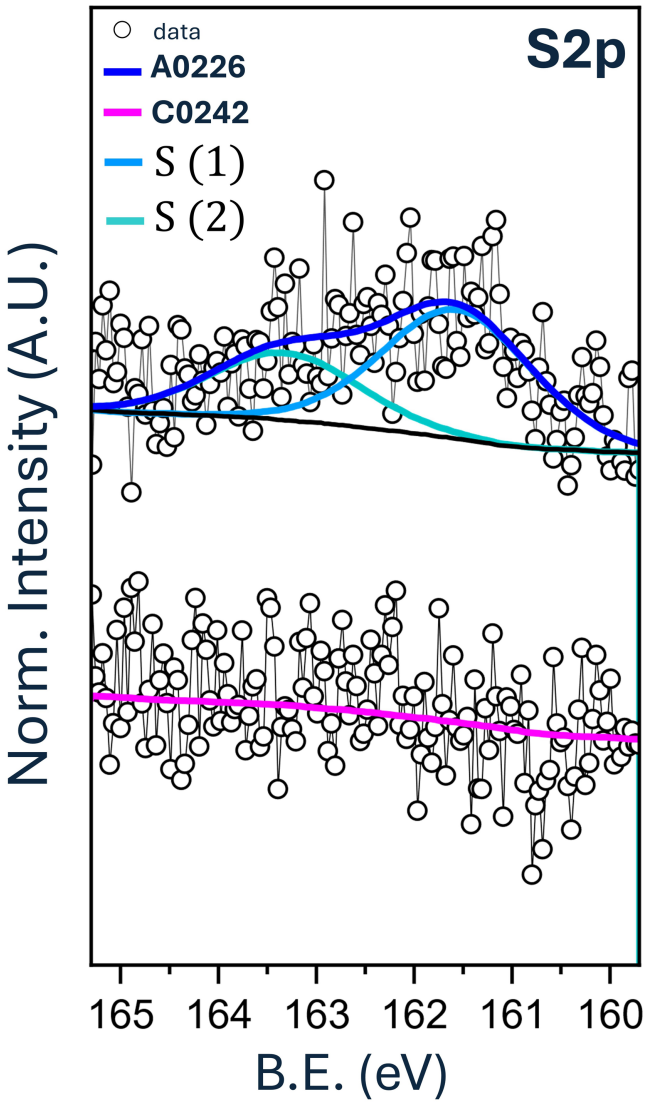

Figure A6. Sulfur (S) 2p photoelectron spectra comparison. Normalized high-resolution S 2p photoelectron spectra of C0242 and A0226 particles. The grain A0226 shows a weak S 2p signal composed of at least two components: one attributable to a reduced sulfur species (S(1), likely S^{2-}) and another at higher BE, consistent with more oxidized sulfur specie [S(2)]. Under the same experimental conditions, these spectral features were not detected on the C0242 particle.

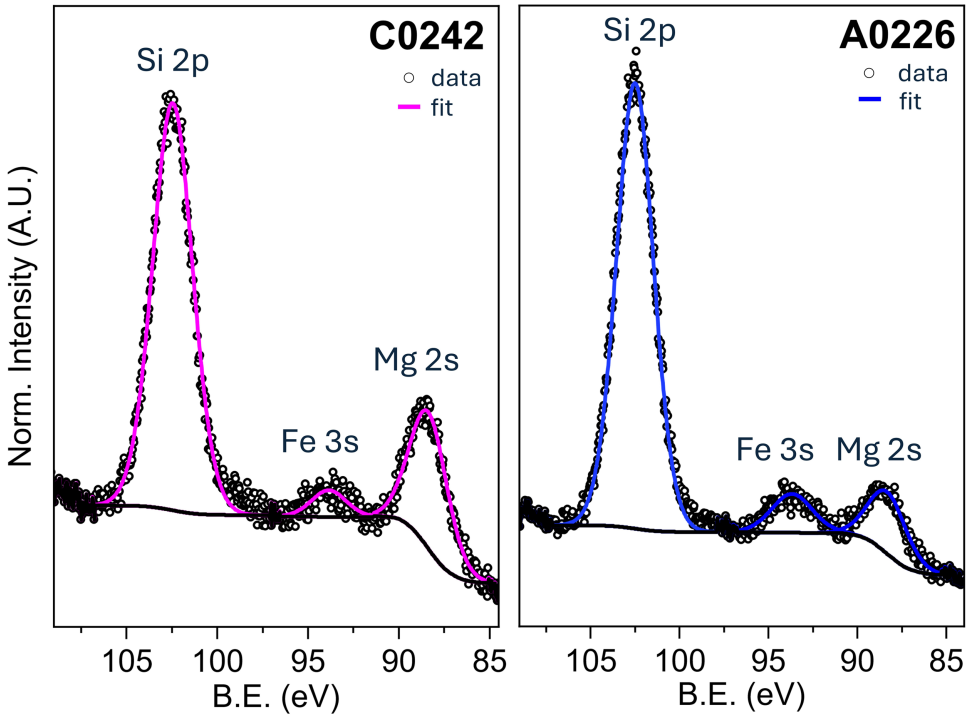

Figure A7. Silicon (Si), iron (Fe), and magnesium (Mg) photoelectron spectra comparison. Normalized high-resolution Si 2p, Fe 3s, and Mg 2s photoelectron spectra of C0242 and A0226 particles.

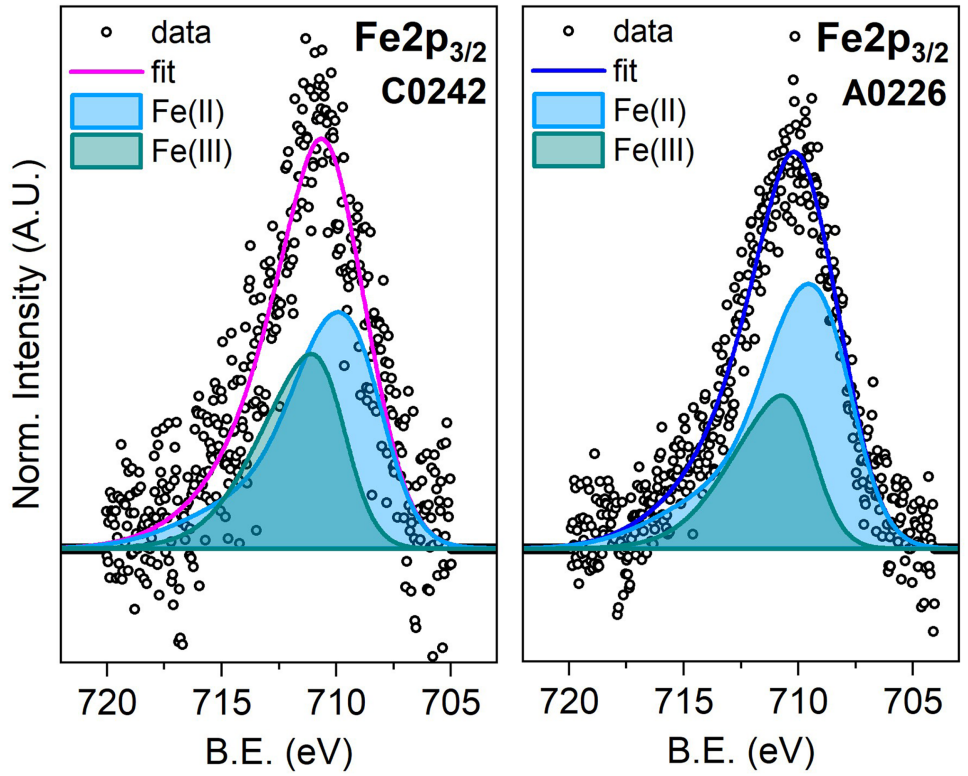

Figure A8. Comparison of iron photoelectron spectra. Normalized high-resolution Fe $2p_{3/2}$ photoelectron spectra of C0242 and A0226 particles. The Fe $2p_{3/2}$ peak for A0226 is slightly shifted toward low BE compared to C0242. A decrease of about 10% in the $Fe^{3+}/\Sigma Fe_{tot}$ ratio for the A0226 was estimated using the procedure of Biesinger et al. (2015), suggesting a more reduced environment on the A0226 surface.

ORCID iDs

E. Palomba https://orcid.org/0000-0002-9101-6774
M. Angrisani https://orcid.org/0000-0002-2178-521X

References

Anand, M., Taylor, L. A., Nazarov, M. A., et al. 2004, PNAS, 101, 6847
Biesinger, M. C., Payne, B. P., Grosvenor, A. P., et al. 2011, ApSS, 257, 2717
Chastain, J., & King, R. C., Jr. 1992, Handbook of X-ray Photoelectron Spectroscopy: A Reference Book of Standard Spectra for Identification and Interpretation of XPS Data, Vol. 40 (Perkin-Elmer Corporation), 221
Christoph, J. M., Minesinger, G. M., Bu, C., Dukes, C. A., & Elkins-Tanton, L. T. 2022, JGRE, 127, e06916
Clark, B. E., Hapke, B., Pieters, C., & Britt, D. 2002, Asteroids III (Univ. of Arizona Press), 585
Denevi, B. W., Noble, S. K., Christoffersen, R., et al. 2023, RvMG, 89, 611
Dukes, C. A., Chang, W. Y., Famá, M., & Baragiola, R. A. 2011, Icar, 212, 463
Elmi, C., Guggenheim, S., & Gieré, R. 2016, CCM, 64, 537
Fulvio, D., Fuks Maron, L., Cires Perez, Y., Tahir, & Del Rosso, T. 2021, Icar, 366, 114532
Hamann, C., Fazio, A., Ebert, M., et al. 2018, M&PS, 53, 1594
Hapke, B. 2001, JGRE, 106, 10039
Harries, D., Matsumoto, T., Langenhorst, F., et al. 2024, M&PS, 59, 2134
Hui, M. T. 2023, AJ, 165, 94
Ito, M., Tomioka, N., Uesugi, K., et al. 2020, EP&S, 72, 133
Jenniskens, P. 2006, Meteor Showers and Their Parent Comets (Cambridge Univ. Press), 6
Jenniskens, P. 2017, P&SS, 143, 116
Keller, L. P., & McKay, D. S. 1993, Sci, 261, 1305
Keller, L. P., Berger, E. L., Zhang, S., & Christoffersen, R. 2021, M&PS, 56, 1685
Killen, R. M. 2003, M&PS, 38, 383
Laczniak, D. L., Thompson, M. S., Christoffersen, R., et al. 2021, Icar, 364, 114479
Laczniak, D. L., Thompson, M. S., Christoffersen, R., et al. 2024, Icar, 410, 115883
Laforet, S., Le Guillou, C., de la Peña, F., et al. 2024, ApJL, 963, L45
Loeffler, M. J., Dukes, C. A., & Baragiola, R. A. 2009, JGRE, 114, E03003
López-Oquendo, A. J., Loeffler, M. J., & Trilling, D. E. 2024, PSJ, 5, 117
Matsumoto, T., Harries, D., Langenhorst, F., et al. 2020, NatCo, 11, 1117
Matsumoto, T., Hasegawa, S., Nakao, S., Sakai, M., & Yurimoto, H. 2018, Icar, 303, 22
Matsumoto, M., Matsuno, J., Tsuchiyama, A., et al. 2024, SciA, 10, eadi7203
Matsuoka, M., Nakamura, T., Hiroi, T., Okumura, S., & Sasaki, S. 2020, ApJL, 890, L23
Matsumoto, T., Noguchi, T., Tobimatsu, Y., et al. 2021, GeCoA, 299, 69
Nakato, A., Yada, T., Nishimura, M., et al. 2023, EP&S, 75, 45
Nittler, L. R., Starr, R. D., Lim, L., et al. 2001, M&PS, 36, 1673
Noble, S. K., Hiroi, T., & Keller, L. P. 2011, LPSC, 42, 1608
Noguchi, T., et al. 2011, Sci, 333, 1121
Noguchi, T., Matsumoto, T., Miyake, A., et al. 2023, NatAs, 7, 170
Okazaki, R., Marty, B., Busemann, H., et al. 2023, Sci, 379, eabo0431
Pieters, C. M., & Noble, S. K. 2016, JGRE, 121, 1865
Shehaj, X., Pratesi, G., Caporali, S., et al. 2025, EP&S, 77, 108
Shirley, D. A. 1972, PhRvB, 5, 4709
Thompson, M. S., Christoffersen, R., Zega, T. J., & Keller, L. P. 2014, EP&S, 66, 89
Tomioka, N., Yamaguchi, A., Ito, M., et al. 2023, NatAs, 7, 669
Watanabe, S., Tsuda, Y., Yoshikawa, M., et al. 2017, SSRv, 208, 3
Wood, B. J., Smythe, D. J., & Harrison, T. 2019, AmMin, 104, 844
Wu, Y., Li, X., Yao, W., & Wang, S. 2017, JGRE, 122, 1956
Yada, T., Abe, M., Okada, T., et al. 2022, NatAs, 6, 214
Yamaguchi, A., Tomioka, N., Ito, M., et al. 2023, NatAs, 7, 398
Zhang, Q., Battams, K., Ye, Q., Knight, M., & Schmidt, C. A. 2023, PSJ, 4, 23